Improving Accuracy of Optical Sorters Using Closed-Loop Control of Material Recirculation

Jonathan Vieth, Marcel Reith-Braun, Albert Bauer, Florian Pfaff, Georg Maier, Robin Gruna, Thomas Längle, Harald Kruggel-Emden, and Uwe D. Hanebeck

***Abstract*— Optical sorting is a key technology for the circular economy and is widely applied in the food, mineral, and recycling industries. Despite its widespread use, one typically resorts to expensive means of adjusting the accuracy, e.g., by reducing the mass flow or changing mechanical or software parameters, which typically requires manual tuning in a lengthy, iterative process. To circumvent these drawbacks, we propose a new layout for optical sorters along with a controller that allows re-feeding of controlled fractions of the sorted mass flows. To this end, we build a dynamic model of the sorter, analyze its static behavior, and show how material recirculation affects the sorting accuracy. Furthermore, we build a model predictive controller (MPC) employing the model and evaluate the closed-loop sorting system using a coupled discrete element–computational fluid dynamics (DEM–CFD) simulation, demonstrating improved accuracy.**

I. Introduction

In optical sorting, we aim to separate particles of different classes. For this purpose, a camera analyzes the particle flow on a transport unit, such as a conveyor belt or chute. Then, a separation unit, typically equipped with nozzles for compressed air, removes particles of undesired classes. Common applications of optical sorters are in the food [1], [2], [3], mineral [4], [5], and recycling industries. Here, optical sorting constitutes a key technology for waste processing [6].

Usually, particles are divided into two classes, resulting in two mass flows after the separation, one for the accepted (positive) particles and one for the rejected (negative) particles. Both contain correctly sorted particles, i.e., true positives (TPs) or true negatives (TNs), and incorrectly sorted particles, i.e., false positives (FPs) or false negatives (FNs). Depending on the application, the goal to achieve is a high true negative rate $\mathrm{TNR} = \mathrm{TN}/(\mathrm{FP}+\mathrm{TN})$ or a high true positive rate $\mathrm{TPR} = \mathrm{TP}/(\mathrm{TP}+\mathrm{FN})$ while maintaining an acceptable TPR or TNR, respectively. The former is typically the case when removing contaminants is crucial, such as in food processing, whereas the latter is of importance when particles to be accepted are of high value, e. g., in diamond sorting [5]. Besides the results of the image processing and the properties of the separation unit, TNR and TPR are mainly affected by the type of particles, the mass flow processed, and the mixing ratio between the classes [7].

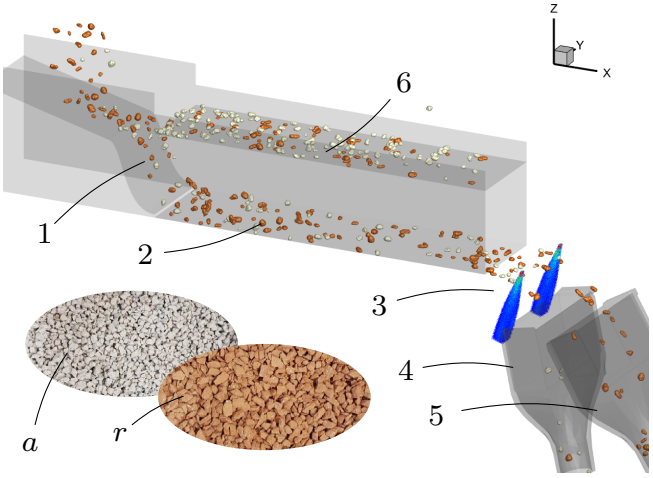

Fig. 1: DEM–CFD model of the sorting system with controlled material recirculation. The mass flow to be sorted is fed onto the feeding chute (1) and then transported by the lower of the two conveyor belts (2) to the nozzles (3) while being analyzed by a camera (not displayed) mounted above the belt (2). The nozzles eject particles of undesired classes into the reject hopper (4) using bursts of compressed air, while accepted particles fly into the accept hopper (5). Controlled fractions of the sorted particles are then immediately repositioned from the hoppers (4), (5) onto the upper belt (6), which models the material recirculation, and returned to the chute (1). We use particle models of sandstone (a) as the accepted material and brick (r) as the rejected material. The particles have diameters from 4 to $8\,\mathrm{mm}$.

While optical sorting has been the subject of intensive research mainly focusing on particle classification [8] and ejection time and location prediction [9], [10], to the best of our knowledge, no research has been conducted w.r.t. the optimization of the TNR and TPR by directly manipulating mass flow or mixing ratio. The trade-off between TNR and TPR is usually accomplished by manually altering system parameters, such as the deflection pattern [9] prior to the actual sorting process. Besides being costly and not guaranteeing the desired accuracy during deployment, the impact of manual adjustments is limited as it is often not

The IGF project 20354 N of the research association Forschungs-Gesellschaft Verfahrens-Technik e.V. (GVT) was supported via the AiF in a program to promote the Industrial Community Research and Development (IGF) by the Federal Ministry for Economic Affairs and Climate Action on the basis of a resolution of the German Bundestag. *(Corresponding author: Marcel Reith-Braun.)*

Jonathan Vieth was with the Intelligent Sensor-Actuator-Systems Laboratory, Karlsruhe Institute of Technology, 76131 Karlsruhe, Germany. He is now with the Institute of Engineering Thermodynamics, Hamburg University of Technology, 21073 Hamburg, Germany (e-mail: jonathan.vieth@tuhh.de).

Marcel Reith-Braun, Florian Pfaff, and Uwe D. Hanebeck are with the Intelligent Sensor-Actuator-Systems Laboratory (ISAS), Karlsruhe Institute of Technology, 76131 Karlsruhe, Germany (e-mail: marcel.reith-braun@kit.edu; pfaff@kit.edu; uwe.hanebeck@kit.edu).

Albert Bauer and Harald Kruggel-Emden are with the Chair of Mechanical Process Engineering and Solids Processing (MVTA), Technical University of Berlin, 10587 Berlin, Germany (e-mail: a.bauer@tu-berlin.de; kruggel-emden@tu-berlin.de).

Georg Maier, Robin Gruna, and Thomas Längle are with the Fraunhofer Institute of Optronics, System Technologies and Image Exploitation (IOSB), 76131 Karlsruhe, (e-mail: georg.maier@iosb.fraunhofer.de; robin.gruna@iosb.fraunhofer.de; thomas.laengle@iosb.fraunhofer.de).

possible to achieve the desired accuracy without reducing mass flow. When high accuracy is required, cascades of sorters can be employed to successively refine the purity of the accepted or rejected mass flow [5]. However, this results in large and expensive plants and still does not provide control over TNR and TPR.

Contribution: To address the aforementioned problems, we propose a novel setup for optical sorters that includes i) a material recirculation added to the optical sorter and ii) a closed-loop controller. In combination, this allows returning a controlled fraction of both the accepted and rejected mass flow to the inlet of the sorter (as illustrated in Fig. 1) and thus direct controlling and optimizing of TNR and TPR. Second, we analyze the system's static behavior and identify scenarios where material recirculation improves sorting accuracy. Third, we evaluate our approach using a DEM–CFD simulation and show improved accuracy of the sorting system as measured by an application-dependent value function.[1]

Paper Overview: We recap the literature on optical sorting and DEM–CFD in Sec. II. In Sec. III, we model the system and identify its parameters based on a DEM–CFD simulation. In Sec. IV, we analyze the system with a focus on its static behavior and propose an MPC in Sec. V. Finally, we present our results in Sec. VI and conclude in Sec. VII.

II. Fundamentals and State of the Art

A. State of the Art in Optical Sorting

One of the most important current applications of optical sorters is in recycling, for recovering light materials such as polymers, rubber, or paper [6]. As data acquisition and processing have vastly increased, recent developments move toward data analysis and machine learning for system improvement [8], [11]. A recently published work presents the application of a mixture-of-experts approach for particle tracking and prediction in optical sorting [10]. As far as the analysis of the overall sorting system is concerned, only little research was done on the experimental [4], [7] and numerical sides [12], [13] using, e. g., DEM–CFD.

B. Coupled Discrete Element Method

The discrete element method is a simulation technique in which particle–particle and particle–wall interactions are resolved in detail. It is able to handle systems with large particle amounts and is often coupled with other simulation methods, such as computational fluid dynamics (CFD), to model a fluid phase surrounding the particles. The fundamental equations describing the particle motion are given by Newton's law of motion and Euler's equation

$$m_i \ddot{\underline{x}}_i = \underline{f}_j^{\mathrm{c}} + \underline{f}_i^{\mathrm{g}} + \underline{f}_i^{\mathrm{f}} \ , \qquad \mathbf{I}_i \dot{\underline{w}}_i + \underline{w}_i \times (\mathbf{I}_i \underline{w}_i) = \underline{M}_j \ ,$$

with the contact forces $\underline{f}_j^{\mathrm{c}}$, the gravitational force $\underline{f}_i^{\mathrm{g}}$, and the fluid forces $\underline{f}_i^{\mathrm{f}}$ causing the acceleration $\ddot{\underline{x}}_i$ on ith body with mass m_i. The angular velocity $\underline{w}_i$ and angular acceleration $\dot{\underline{w}}_i$ of particle i result from external moments $\underline{M}_j$. Here, $\mathbf{I}_i$ is the inertia tensor given in the principal coordinate system. In the CFD, the Navier–Stokes equations are solved. The relative velocity between fluid and particles imposes forces on the particles. DEM–CFD was recently used to model an optical belt sorter [13]. The authors employ a one-way coupling method, which means that the fluid field is not perturbed by the particles.

[1] Our source code is available at `https://github.com/KIT-ISAS/ControlledRecirculation`

III. Modeling and Identification

In a first step, we model the system without recirculation and identify its parameters by using data from a DEM–CFD simulation. The second part of the chapter addresses the modeling of the system with recirculation, as displayed in Fig. 2. The recirculation comprises an additional device, referred to as the recirculation unit, whose task is to return partial mass flows of both the accepted and rejected particles.

The model is based on the law of mass conservation. In order to develop an adequate model for the synthesis of controllers, the particle-specific motion is neglected and transport processes are simply described by time delays.

A. Model of the System without Recirculation

1) Modeling: The transport process on the transport unit is described based on the estimated time a particle takes to travel from the beginning of the transport unit to the center of the camera field of view τ_{RQ} and the estimated travel time from the center of the camera field of view to the separation unit τ_{QS} (see Fig. 2). The mass flow $\underline{q}(t) = \begin{bmatrix} q_{\mathrm{P}}(t) & q_{\mathrm{N}}(t) \end{bmatrix}^\top$, as measured by the camera above the transport unit, depends only on the input mass flow $\underline{r}(t) = \begin{bmatrix} r_{\mathrm{P}}(t) & r_{\mathrm{N}}(t) \end{bmatrix}^\top$ via $\underline{q}(t) = \underline{r}(t - \tau_{\mathrm{RQ}})$. Here, $\underline{q}(t)$ and $\underline{r}(t)$ consist of the mass flows of the accept and reject particles (indicated by the indices P and N, respectively).

The separation unit can be understood as a static nonlinearity $\underline{f} \colon \mathbb{R}^2_{\geq 0} \to \mathbb{R}^4_{\geq 0}$ mapping $\underline{q}(t)$ to the mass flow at the outlet of the sorter $\underline{y} = \begin{bmatrix} y_{\mathrm{TP}}(t) & y_{\mathrm{FP}}(t) & y_{\mathrm{FN}}(t) & y_{\mathrm{TN}}(t) \end{bmatrix}^\top$, in which the components of $\underline{y}$ represent the mass flows of TPs, FPs, FNs, and TNs, respectively. Again, we model the travel time from the separation unit to the sorter outlet by a time delay τ_{SY}. With $\tau_{\mathrm{QY}} = \tau_{\mathrm{QS}} + \tau_{\mathrm{SY}}$ and $\underline{f}$ being the product of $\underline{q}(t)$ with a $\underline{q}(t)$-dependent matrix $\mathbf{\Gamma}(\underline{q}(t))$, we arrive at

$$\underline{y}(t + \tau_{\mathrm{QY}}) = \mathbf{\Gamma}(\underline{q}(t))\underline{q}(t) \ , \tag{1}$$

$$\mathbf{\Gamma}(\underline{q}(t)) = \begin{bmatrix} \epsilon(\underline{q}(t)) & 0 \\ 0 & (1 - \zeta(\underline{q}(t))) \\ (1 - \epsilon(\underline{q}(t))) & 0 \\ 0 & \zeta(\underline{q}(t)) \end{bmatrix} \ ,$$

in which the potentially nonlinear functions $\epsilon \colon \mathbb{R}^2_+ \to (0, 1)$ and $\zeta \colon \mathbb{R}^2_+ \to (0, 1)$ can be understood as the TPR and the TNR of the separation unit, respectively.

2) Identification: For estimating $\epsilon(\underline{q}(t))$ and $\zeta(\underline{q}(t))$, we assume that quadratic polynomials

$$\epsilon(\underline{q}) = o_{00} + o_{10} q_{\mathrm{P}} + o_{01} q_{\mathrm{N}} + o_{20} q_{\mathrm{P}}^2 + o_{11} q_{\mathrm{P}} q_{\mathrm{N}} + o_{02} q_{\mathrm{N}}^2, \tag{2a}$$

$$\zeta(\underline{q}) = z_{00} + z_{10} q_{\mathrm{P}} + z_{01} q_{\mathrm{N}} + z_{20} q_{\mathrm{P}}^2 + z_{11} q_{\mathrm{P}} q_{\mathrm{N}} + z_{02} q_{\mathrm{N}}^2 \tag{2b}$$

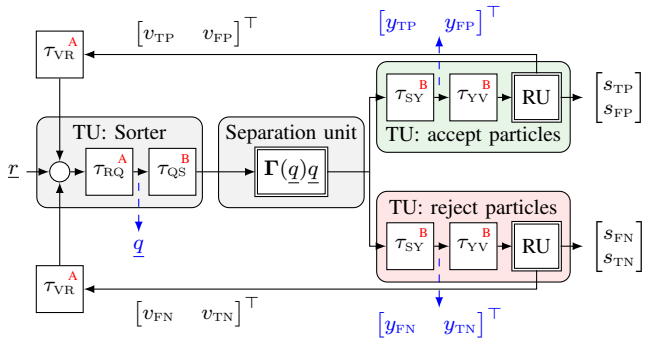

Fig. 2: General layout of a sorting system with recirculation. Time delays are denoted by $\tau_a, a \in \{\mathrm{RQ}, \mathrm{QS}, \mathrm{SY}, \mathrm{YV}, \mathrm{VR}\}$. Time delays with the upper index A or B are part of the cumulative delays τ_{A} or τ_{B}, respectively. The nonlinear block RU describes the recirculation unit, as described by (4). TU stands for transport unit. Measurement vectors are highlighted in blue, and the time dependencies of all vectors are omitted for simplicity.

are sufficient as this facilitates generating quadratic objective functions. To identify the parameters, we conducted several DEM–CFD simulations using a sorter model based on the work [13]. The simulated material was demolition waste consisting of two fractions, as displayed in Fig. 1. We used a prediction straight along the transparent direction to calculate the nozzle activation times. The particle velocity is assumed to be equal to the belt velocity. The activation time is then calculated using a constant velocity model. In extension to [13], the number of nozzles to activate was determined according to the particle width, so that one to three nozzles were activated per particle. The activation duration was fixed at $10\,\mathrm{ms}$. The virtual observation line for localization and classification of the particles was at the belt edge. We considered static mass flows $m(t) = q_{\mathrm{P}}(t) + q_{\mathrm{N}}(t)$ between $10\,\mathrm{g\,s^{-1}}$ and $250\,\mathrm{g\,s^{-1}}$ and static accept particles shares $a(t) = {}^{q_{\mathrm{P}}(t)}/_{m(t)}$ between $50\,\%$ and $97\,\%$. In order to reduce the number of numerical experiments required, we assume that for $a < 0.5$, $\mathrm{TPR}(m, a) = \mathrm{TNR}(m, 1-a)$ and $\mathrm{TNR}(m, a) = \mathrm{TPR}(m, 1-a)$ since one can switch from ejecting reject to ejecting accept particles for $a < 0.5$.

As shown in Fig. 3, the quadratic polynomials fit the measured data well. However, due to the unbounded nature of quadratic polynomials, there are regions in which $\epsilon(\underline{q})$ and $\zeta(\underline{q})$ are larger than one or less than zero, which is not admissible and must be considered in the further course. The parameters of (2) are given in Tab. I.

B. Adding the Material Recirculation

The recirculation unit returns a partial mass flow $\underline{v} = \begin{bmatrix} v_{\mathrm{TP}}(t) & v_{\mathrm{FP}}(t) & v_{\mathrm{FN}}(t) & v_{\mathrm{TN}}(t) \end{bmatrix}^\top$ to the sorter inlet (see Fig. 2). Hence, the new output mass flow of the system $\underline{s}(t) = \begin{bmatrix} s_{\mathrm{TP}}(t) & s_{\mathrm{FP}}(t) & s_{\mathrm{FN}}(t) & s_{\mathrm{TN}}(t) \end{bmatrix}^\top$ is given by

$$\underline{s}(t) = \underline{y}(t - \tau_{\mathrm{YV}}) - \underline{v}(t) \ , \tag{3}$$

in which the indices of $\underline{v}(t)$ and $\underline{s}(t)$ again denote TPs, FPs, FNs, and TNs and τ_{YV} is the estimated time it takes for a particle to move from the outlet of the sorter to the recirculation unit. By denoting the fractions of the mass flows

TABLE I: Identified parameters of the functions ϵ and ζ multiplied by 10^4

Parameter	00	10	01	20	11	02
$\epsilon(\underline{q})$	9995	-5.625	-0.669	0.0288	-0.0468	0.0577
$\zeta(\underline{q})$	9950	-2.466	-2.33	0.0158	-0.0487	0.0116

of accept and reject particles to be returned by $u_{\mathrm{P}}, u_{\mathrm{N}} \in [0, 1]$ and under the assumption that $y_{\mathrm{TP}}(t)$ and $y_{\mathrm{FP}}(t)$ are equally affected by u_{P}, and analogously that u_{N} affects $y_{\mathrm{FN}}(t)$ and $y_{\mathrm{TN}}(t)$ equally, $\underline{v}(t)$ is given by

$$\underline{v}(t) = \mathbf{U}(\underline{u}(t))\underline{y}(t - \tau_{\mathrm{YV}}) \ , \tag{4}$$
$$\mathbf{U}(\underline{u}(t)) = \mathrm{Diag}\left\{\mathbf{M}^\top \underline{u}(t)\right\} \ , \quad \mathbf{M} = \begin{bmatrix} 1 & 1 & 0 & 0 \\ 0 & 0 & 1 & 1 \end{bmatrix} \ ,$$

with $\underline{u}(t) = \begin{bmatrix} u_{\mathrm{P}}(t) & u_{\mathrm{N}}(t) \end{bmatrix}^\top$ being the vector of control signals. Consequently, the new mass flow on the belt is

$$\underline{q}(t + \tau_{\mathrm{A}}) = \mathbf{N}\underline{v}(t) + \underline{r}(t + \tau_{\mathrm{VR}}) \ , \tag{5}$$
$$\mathbf{N} = \begin{bmatrix} 1 & 0 & 1 & 0 \\ 0 & 1 & 0 & 1 \end{bmatrix} \ ,$$

with $\tau_{\mathrm{A}} = \tau_{\mathrm{VR}} + \tau_{\mathrm{RQ}}$ and τ_{VR} being the travel time from the recirculation unit to the mixing point with $\underline{r}(t)$.

Thus, the system with recirculation is characterized completely by (1), (3), (4), and (5). From now on, we further assume that we can measure $\underline{y}(t)$, as depicted in Fig. 2.

IV. System Analysis

The system without recirculation can be understood as a subclass of a *Wiener-type nonlinear system*, i.e., a block-oriented model that consists of a time-delayed linear dynamic part followed by a nonlinear memoryless function [14]. In our case, the linear part is given by the pure time delays τ_{RQ}, τ_{QY} and the nonlinear function corresponds to the separation unit. However, the system with recirculation is not Wiener-type due to its nonlinear dynamics. In addition, the systems with and without recirculation are solely time-delayed systems without any integrating or differentiating parts. Thus, no continuous-time state-space representation can be obtained.

In general, the recirculation affects the accuracy of the sorting process via two effects:

E1: by adding particles to the transport unit,
E2: by removing particles after the separation unit.

E1 can be understood as a change of the operation point of the separation unit towards higher mass flows, which, depending on the current operation point and the form of $\epsilon(\overline{q})$ and $\epsilon(\overline{q})$, may lead to improved accuracy. E2 directly alters the output equation (3) and thus has a direct influence on the system's TNR and TPR. We will examine E2 and the combination of E1 and E2 more closely in the next paragraphs, where we study the steady-state behavior of the system with recirculation.

A. Steady-State Analysis Ignoring E1

We will now study the steady-state behavior of the system, i.e., $\underline{q}(t) = \overline{q}$, $\underline{u}(t) = \overline{u}$, $\underline{r}(t) = \overline{r}$, $\underline{s}(t) = \overline{s}$, with constant but unknown $\overline{q}$, $\overline{u}$, $\overline{r}$, $\overline{s}$ (all time delays can be omitted). In a first step, we ignore E1 and solely study the impact of E2.

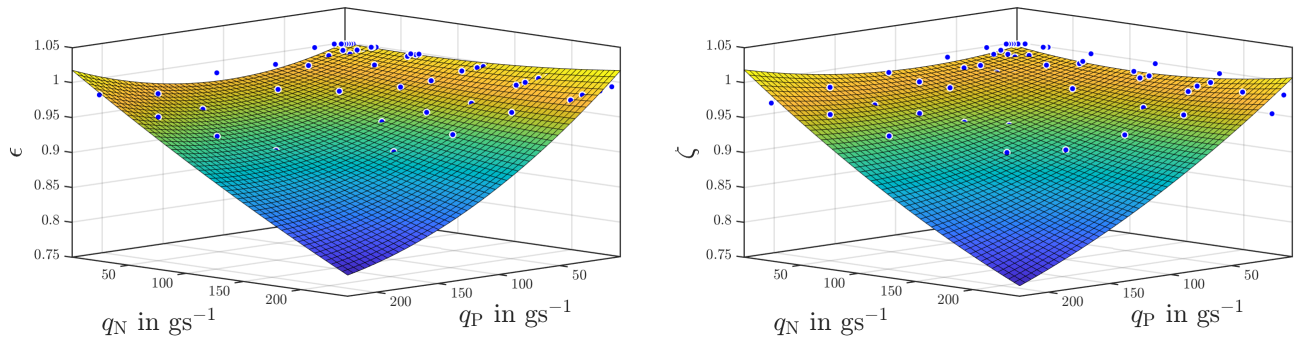

(a) TPR

(b) TNR

Fig. 3: Fitted curves for the TPR and TNR of the separation unit, i.e., the sorter without recirculation. The blue points are the TPR and TNR values obtained from the DEM–CFD simulations. The sum of squares fitting error of the TPR is 0.0045 and for the TNR, it is 0.0151.

Assumption 1. The effect of $\underline{q}$ and hence of $\underline{u}$ on (2) can be neglected so that $\epsilon(\underline{\overline{q}}) = \overline{\epsilon}$ and $\zeta(\underline{\overline{q}}) = \overline{\zeta}$ with arbitrary constants $\overline{\epsilon}$, $\overline{\zeta} \in (0, 1)$.

Proposition 1. Consider the system described by (1), (3), (4), and (5) in steady state. Suppose that Assumption 1 holds. Then, with a fixed $\overline{u}_\mathrm{N} \in [0, 1)$, the TNR is a strictly monotonically increasing function in $\overline{u}_\mathrm{P}$ and, with a fixed $\overline{u}_\mathrm{P} \in [0, 1)$, the TNR is a strictly monotonically decreasing function in $\overline{u}_\mathrm{N}$. The converse applies to the TPR.

Proof. Due to Assumption 1, $\mathbf{\Gamma}(\underline{\overline{q}}) = \overline{\mathbf{\Gamma}}$ is now a constant matrix. Hence, (1), (4), and (5) can be solved for $\underline{\overline{q}}$, which results in $\underline{\overline{q}} = \left(\mathbf{I} - \mathbf{NU}\left(\underline{\overline{u}}\right)\overline{\mathbf{\Gamma}}\right)^{-1}\underline{\overline{r}}$. Using (3), we arrive at the steady-state TPR and TNR

$$\overline{\mathrm{TPR}}(\underline{\overline{u}}) := \frac{\overline{s}_\mathrm{TP}}{\overline{s}_\mathrm{TP} + \overline{s}_\mathrm{FN}} = \frac{\overline{\epsilon}(1 - \overline{u}_\mathrm{P})}{1 - \overline{u}_\mathrm{N}(1 - \overline{\epsilon}) - \overline{u}_\mathrm{P}\overline{\epsilon}} \ ,$$
$$\overline{\mathrm{TNR}}(\underline{\overline{u}}) := \frac{\overline{s}_\mathrm{TN}}{\overline{s}_\mathrm{TN} + \overline{s}_\mathrm{FP}} = \frac{\overline{\zeta}(1 - \overline{u}_\mathrm{N})}{1 - \overline{u}_\mathrm{P}(1 - \overline{\zeta}) - \overline{u}_\mathrm{N}\overline{\zeta}} \ .$$

$\nabla\overline{\mathrm{TNR}}$ equals $\frac{\overline{\zeta}(1-\overline{\zeta})}{\left(1-\overline{u}_\mathrm{P}(1-\overline{\zeta})-\overline{u}_\mathrm{N}\overline{\zeta}\right)^2}\begin{bmatrix}1-\overline{u}_\mathrm{N} & \overline{u}_\mathrm{P}-1\end{bmatrix}^\top$ and thus, the first component (for $\overline{u}_\mathrm{P}$) is always positive and the second component (for $\overline{u}_\mathrm{N}$) is always negative since $\overline{u}_\mathrm{P}, \overline{u}_\mathrm{N} \in [0, 1)$, $\overline{\epsilon}, \overline{\zeta} \in (0, 1)$ and because the denominator is always greater than zero. The proof for the TPR follows analogously. ■

Note that returning only one fraction, either of the mass flow of accepted or rejected particles, increases the $\overline{\mathrm{TNR}}$ or $\overline{\mathrm{TPR}}$ compared with the system without recirculation ($\underline{\overline{u}} = \underline{0}$), respectively. However, increasing the $\overline{\mathrm{TNR}}$ always causes a decrease of the $\overline{\mathrm{TPR}}$ and vice versa. For $\overline{\epsilon} = 0.97$ and $\overline{\zeta} = 0.98$, $\overline{\mathrm{TNR}}$, $\overline{\mathrm{TPR}}$, and the objective function $\overline{J}(\underline{\overline{u}}) = 0.5\overline{\mathrm{TPR}}(\underline{\overline{u}}) + 0.5\overline{\mathrm{TNR}}(\underline{\overline{u}})$ are displayed in Fig. 4 as functions of $\underline{\overline{u}}$. The dotted line in Fig. 4c represents the set of optimal control variables $\overline{u}^*_\mathrm{P}$ and $\overline{u}^*_\mathrm{N}$, obtained by maximizing $\overline{J}(\underline{\overline{u}})$,

$$\overline{u}^*_\mathrm{N} = 1 + (\overline{u}^*_\mathrm{P} - 1)\sqrt{\frac{\overline{\epsilon}(\overline{\zeta}-1)}{\overline{\zeta}(\overline{\epsilon}-1)}} \ , \quad 1 - \sqrt{\frac{\overline{\zeta}-\overline{\epsilon}\overline{\zeta}}{(1-\overline{\zeta})\overline{\epsilon}}} < \overline{u}^*_\mathrm{P} < 1 \ .$$

B. Steady-State Analysis Considering Both Effects

Since $\overline{\epsilon}$ and $\overline{\zeta}$ are in general functions of $\underline{\overline{q}}$ and therefore dependent on $\underline{\overline{u}}$, we now examine the combined influence of both E1 and E2. In this case, it is not possible to solve (1), (4), and (5) for $\underline{\overline{q}}$ analytically. Thus, we use a numerical approach to compute $\overline{\mathrm{TPR}}$ and $\overline{\mathrm{TNR}}$ consisting of the steps

1) span a grid with the control variables $\underline{\overline{u}}$ on the axes,
2) solve (1), (4), and (5) for $\underline{\overline{q}}$ at each point of the grid (note that we therefore need to choose a specific $\underline{\overline{r}}$),
3) fit the two functions $\overline{q}_\mathrm{N}(\underline{\overline{u}})$ and $\overline{q}_\mathrm{P}(\underline{\overline{u}})$,
4) compute $\overline{\mathrm{TPR}}(\underline{\overline{u}})$, $\overline{\mathrm{TNR}}(\underline{\overline{u}})$, and $\overline{J}(\underline{\overline{u}})$.

The results are given in Fig. 5. Comparison of Fig. 4 and Fig. 5 shows that for the chosen $\overline{\epsilon}$ and $\overline{\zeta}$, E2 also appears dominant in the combined case since the basic shapes of the curves are similar in both figures. However, E1 bends the curves according to the nonlinearity.

As a result, when considering E1 and E2, the optimal steady-state control variables depend on $\underline{\overline{r}}$. Furthermore, there is no analytic solution for $\underline{\overline{u}}^*$. Hence, in the next section, we present an MPC that can cope with both challenges.

V. Model Predictive Controller

An MPC uses a system model to predict the future system dynamics and attempts to find a sequence of control variables in each run that minimizes a finite-horizon objective function. Thus, an MPC is able to control the steady-state behavior as well as to cope with dynamic changes. Furthermore, an MPC is particularly suitable for our case because the internal formulation of the control problem as an optimization problem naturally allows us to encode our desired goal of finding the best operating point of the sorting system (note that, unlike many other control problems, we are not interested in reaching a particular set point or following a specific trajectory). Our MPC computes the sequence of control variables starting with $\underline{u}_{k+1}$ at each time step k and applies $\underline{u}_{k+1}$ at $k + 1$, thus leaving enough time for measurement processing and optimization.

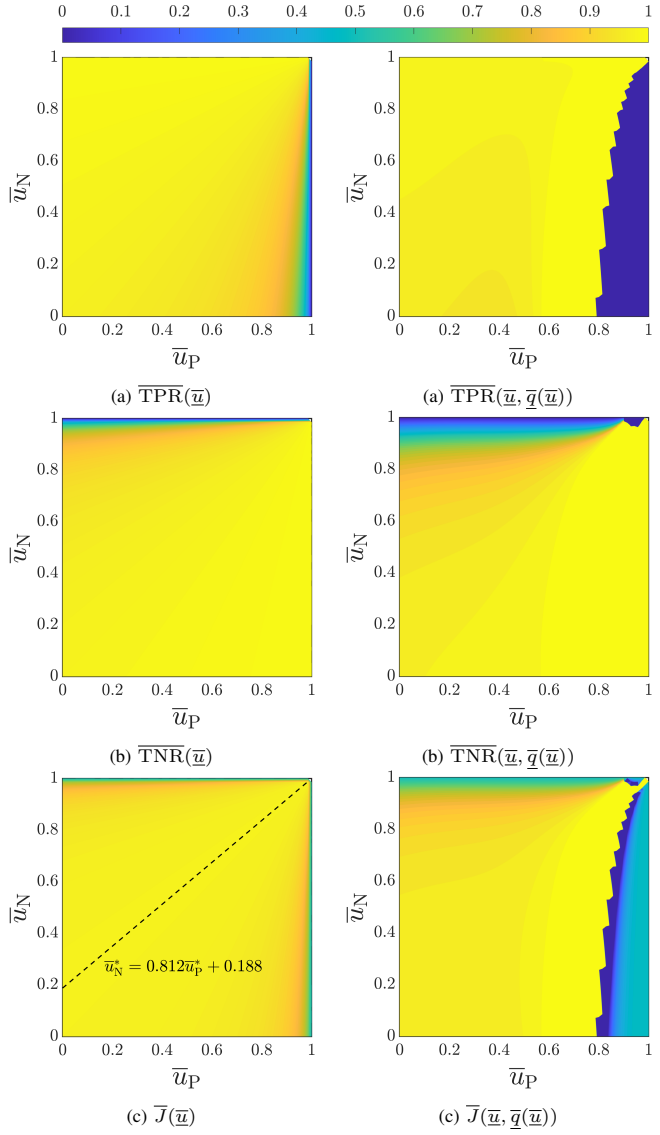

(a) $\overline{\mathrm{TPR}}(\underline{\overline{u}})$ (a) $\overline{\mathrm{TPR}}(\underline{\overline{u}}, \underline{\overline{q}}(\underline{\overline{u}}))$

(b) $\overline{\mathrm{TNR}}(\underline{\overline{u}})$ (b) $\overline{\mathrm{TNR}}(\underline{\overline{u}}, \underline{\overline{q}}(\underline{\overline{u}}))$

(c) $\overline{J}(\underline{\overline{u}})$ (c) $\overline{J}(\underline{\overline{u}}, \underline{\overline{q}}(\underline{\overline{u}}))$

Fig. 4: Objectives for the steady-state behavior of the simplified sorting system in the case of $\overline{\epsilon} = 0.97$ and $\overline{\zeta} = 0.98$ depending on the steady-state control variables $\underline{\overline{u}}$.

Fig. 5: Objectives for the steady-state behavior depending on the steady-state control variables $\underline{\overline{u}}$ in the case of $r_\mathrm{P} = 90\,\mathrm{g\,s^{-1}}$ and $r_\mathrm{N} = 10\,\mathrm{g\,s^{-1}}$.

A. Prediction

By discretizing the system model given by (1), (3), (4), and (5), we obtain the state-space representation

$$\underline{q}_{k+k_\mathrm{A}} = \mathbf{N}\mathbf{U}(\underline{u}_k)\mathbf{\Gamma}(\underline{q}_{k-k_\mathrm{B}})\underline{q}_{k-k_\mathrm{B}} + \underline{r}_{k+k_\mathrm{VR}} \quad , \tag{6a}$$

$$\underline{s}_k = (\mathbf{I} - \mathbf{U}(\underline{u}_k))\,\mathbf{\Gamma}(\underline{q}_{k-k_\mathrm{B}})\underline{q}_{k-k_\mathrm{B}} \quad , \tag{6b}$$

where $k_i \approx {}^{\tau_i}\!/_T, i \in \{\mathrm{A}, \mathrm{B}, \mathrm{VR}\}$ are approximate discrete-time delays with $\tau_\mathrm{B} = \tau_\mathrm{QS} + \tau_\mathrm{SY} + \tau_\mathrm{YV}$. The sampling time T is chosen such that the τ_is are approximately multiples of T. Note that (6) is not in standard form (to obtain it, one can use *state augmentation*, as described in [15]). Related to this, note that under the assumption of constant and known inputs $\underline{r}(t) = \overline{\underline{r}}$, all states of the sequence $\underline{q}_{k+1}, \dots, \underline{q}_{k+k_\mathrm{A}}$ can be predicted solely based on the stored history of measurements of $\underline{q}_{k+1-k_\mathrm{A}-k_\mathrm{B}}, \dots, \underline{q}_{k-k_\mathrm{B}}$ and the known history of control variables $\underline{u}_{k+1-k_\mathrm{A}}, \dots, \underline{u}_k$ without any assumptions on future control variables $\underline{u}_{\tilde{k}}$, $\tilde{k} > k$. Furthermore, all states of the sequence $\underline{q}_{k+k_\mathrm{A}+1}, \dots, \underline{q}_{k+\hat{k}}$, with $\hat{k} = k_\mathrm{A} + k_\mathrm{B}$ being the number of time steps for one cycle, only depend linearly on the future control variables $\underline{u}_{k+1}, \dots, \underline{u}_{k+k_\mathrm{B}}$ and the stored history of measurements of $\underline{q}_{k-k_\mathrm{B}+1}, \dots, \underline{q}_k$. This is a direct consequence of $\underline{u}_k$ only influencing $\underline{q}_{k+k_\mathrm{A}+i\hat{k}}$, $i \in \mathbb{N}_0$ via the state dynamics (6a) and $\underline{s}_{k+i\hat{k}}$ via the output equation (6b). In our MPC, we have additional measurements of $\underline{y}$ via the measurement equation $\underline{y}_{k-k_\mathrm{YV}} = \mathbf{\Gamma}(\underline{q}_{k-k_\mathrm{B}})\underline{q}_{k-k_\mathrm{B}}$, which we can plug directly into (6a). Thus, for predicting $\underline{q}_{k+1}, \dots, \underline{q}_{k+k_\mathrm{A}+k_\mathrm{YV}}$, we use the measurements of $\underline{y}_{k+1-k_\mathrm{A}-k_\mathrm{YV}}, \dots, \underline{y}_k$ and $\underline{u}_{k+1-k_\mathrm{A}}, \dots, \underline{u}_{k+k_\mathrm{YV}}$ instead of the measurements of $\underline{q}$.

B. Optimization

In each time step, the MPC solves the optimization problem

$$\min_{\tilde{\underline{u}}} \left(\sum_{i=k+1}^{k+N} J_i \right) \quad , \quad \text{s.t.} \quad (6a), \quad \underline{0}_{2N} \le \tilde{\underline{u}} \le \underline{1}_{2N},$$

in which $\tilde{\underline{u}}^\top = \begin{bmatrix} \underline{u}_{k+1}^\top & \dots & \underline{u}_{k+N}^\top \end{bmatrix}$ is the sequence of future control variables, J_i the objective function at time step i, k the current time step, and $N \in \mathbb{N}$ the control horizon. Note that the inequality constraints are linear. When choosing the control horizon $N \le \hat{k}$, the equality constraints (6a) are also linear, as previously discussed.

We propose to use a combined objective function

$$J_i^{(\mathrm{E1+E2})} = c^{(\mathrm{E1})} J_i^{(\mathrm{E1})} + c^{(\mathrm{E2})} J_i^{(\mathrm{E2})}$$

that considers both E1 and E2 via the terms $J_i^{(\mathrm{E1})}$ and $J_i^{(\mathrm{E2})}$ and weights $c^{(\mathrm{E1})}, c^{(\mathrm{E2})} \in \mathbb{R}_{\ge 0}$. E2 is taken into account by

$$J_i^{(\mathrm{E2})} = c_\mathrm{P} \frac{s_{\mathrm{TP},i}}{s_{\mathrm{TP},i} + s_{\mathrm{FN},i}} + c_\mathrm{N} \frac{s_{\mathrm{TN},i}}{s_{\mathrm{TN},i} + s_{\mathrm{FP},i}} \quad , \tag{7}$$

with weights $c_\mathrm{P}, c_\mathrm{N} \le 0$. Thus, minimizing $J_i^{(\mathrm{E2})}$ directly maximizes the system's TPR and TNR. E1 is considered by

$$J_i^{(\mathrm{E1})} = c_\epsilon \epsilon(\underline{q}_{i+k_\mathrm{A}}) + c_\zeta \zeta(\underline{q}_{i+k_\mathrm{A}}) \quad ,$$

with weights $c_\epsilon, c_\zeta \le 0$, which directly aims to improve the TPR and TNR of the sorter without recirculation. $J_i^{(\mathrm{E1})}$ is quadratic since (2) is quadratic. Note that $J_i^{(\mathrm{E2})}$ alone (with a large enough N) would be sufficient to optimize the system's TPR and TNR. Nevertheless, it has proven useful to combine both objectives since this allows choosing $N \le \hat{k}$ and thus exploiting linear equality constraints while still considering E1. However, incorporating $J_i^{(\mathrm{E1})}$ generally comes with the drawback that the objective function is no longer quadratic.

VI. Simulation

We evaluate our MPC using a DEM–CFD simulation of the sorting system with recirculation on three different scenarios and compare it with the same sorter without recirculation. For this purpose, we use the DEM–CFD model from Sec. III and integrate a recirculation as shown in Fig. 1. The scenarios

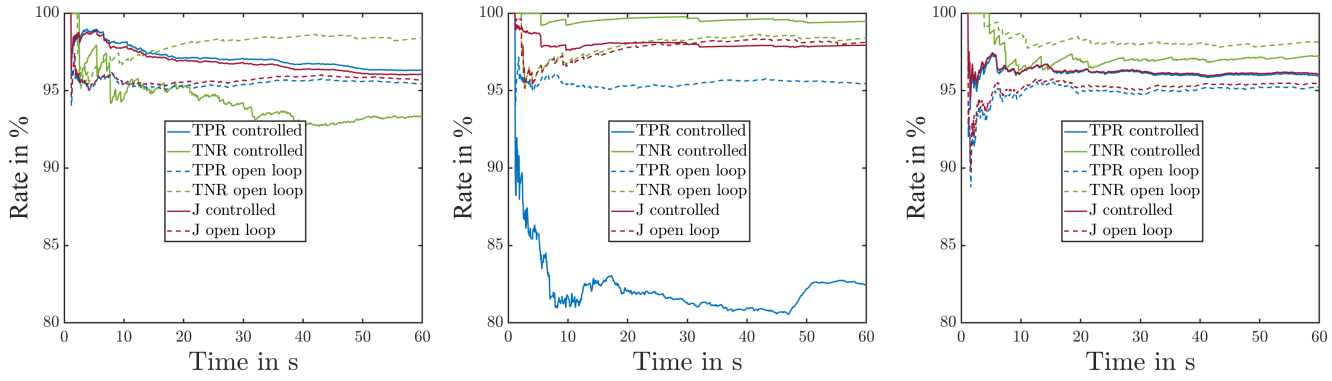

(a) Scenario S1, TPR controlled. (b) Scenario S2, TNR controlled. (c) Scenario S3, TPR controlled.

Fig. 6: Results of controller application to the DEM–CFD simulation model of the optical sorting system with recirculation. Comparison of the uncontrolled system, i.e., the system without material recirculation (dashed) and the controlled system (solid). In red, objective functions J according to (7) are plotted. The curves show the overall sorting accuracies up to the respective point in time, i.e., the accuracies w.r.t. all particles sorted by then.

considered are described by Tab. II. They all have constant mass inflow, i. e., $\underline{r}(t) = \overline{r}$, but vary in the mass flows of incoming accept and reject particles and the weights of the objective function. 60 s are considered in each scenario.

A. Parameters of the MPC

We use the objective function $J_i^{(\mathrm{E1+E2})}$, where $c^{(\mathrm{E1})} = c^{(\mathrm{E2})} = 0.5$, $c_\mathrm{P} = c_\epsilon$, and $c_\mathrm{N} = c_\zeta$. The delays τ_RQ, τ_QS, τ_SY, τ_YV, and τ_VR were set to the approximate delays from the DEM–CFD model: 0.445, 0.125, 0, 0, and 3.7425 s. Following the explanations in Sec. V, the sampling time was set to $T = 62.5\,\mathrm{ms}$ and a control horizon of $N = \hat{k}$ was used in order to ensure linear constraints. The MPC receives measurements of $\underline{y}$ and $\underline{q}$ and knows $\overline{r}$. To smooth high-frequency changes in the measurements of $\underline{y}$, a *moving mean filter* covering ten time steps was applied. The optimization problem was solved in MATLAB by using a built-in *sequential-quadratic programming* method with a constraint tolerance of 1×10^{-2}, an optimality tolerance of 1×10^{-3}, and a step tolerance of 9.9×10^{-5}. In each step, it took the MPC an average of 0.12 s to find the optimal control variables.[2]

B. Results

Fig. 6 presents our simulation results. In scenario S1 (see Fig. 6a), the TPR at 60 s of the controlled system is at 96.3 % compared with 95.4 % of the sorter without recirculation. Thus, the MPC reaches its goal to improve the TPR as determined by the chosen weights. The improvement in the TPR comes with a notable decrease in the TNR from 98.4 % to 93.3 %. The objective function J as computed according to (7), however, lies above J in the uncontrolled case at all times. Thus, the overall sorting performance is gradually higher when controlled by the MPC. If we change the weights, as in S2 (Fig. 6b), the MPC is able to improve the TNR by roughly 1 p.p. to 99.5 %. Again, there is a sharp decline of 13 p.p. in the TPR. Consequently, no improvement in J is achieved. In S3, the mass flow was halved while the fraction of rejects was doubled compared with S1 and S2.

[2]Evaluated with an AMD Ryzen 9 3950X at 3.5 GHz and 32 GB RAM.

TABLE II: Scenarios considered in the simulations

Scenario	$\overline{r}_\mathrm{P}$	$\overline{r}_\mathrm{N}$	$c_\mathrm{P} = c_\epsilon$	$c_\mathrm{N} = c_\zeta$
S1	$90\,\mathrm{g\,s^{-1}}$	$10\,\mathrm{g\,s^{-1}}$	−0.909	−0.091
S2	$90\,\mathrm{g\,s^{-1}}$	$10\,\mathrm{g\,s^{-1}}$	−0.091	−0.909
S3	$40\,\mathrm{g\,s^{-1}}$	$10\,\mathrm{g\,s^{-1}}$	−0.909	−0.091

As with S1, the weights were chosen such that the TPR is improved. While the system without recirculation performs similarly to S1 and S2, controlled recirculation again achieves an increase of roughly 1 p.p. At the same time, the TNR is reduced by nearly 1 p.p. Expressed in terms of J, the summed sorting accuracy is 0.6 p.p. higher if we apply the MPC.

In summary, the application of our proposed MPC to a simulated DEM–CFD sorter model yielded good results. The controller was able to improve the targeted quantity in all analyzed cases. As scenarios S2 and S3 show, even in cases where the targeted quantity was already very high in the uncontrolled case, a further significant improvement can be achieved by controlled recirculation. Again, it can be observed that improving TNR is accompanied by a decrease in TPR and vice versa. Especially if the targeted rate is near optimal, a further increase is connected to a significant loss in the second, not targeted rate.

VII. Conclusion

We proposed a new setup for direct control of TPR and TNR of optical sorters by returning controlled fractions of the sorted mass flows. To this end, we modeled the sorting system as a nonlinear, time-delayed system and showed by analyzing its static behavior that a higher accuracy, as measured by an application-dependent weighted sum of TPR and TNR, can be achieved. However, an improvement in TNR generally comes with a decrease in TPR and vice versa. Moreover, we proposed an MPC for control of the system and showed using a DEM–CFD simulation that even for uncontrolled TNRs or TPRs greater than 95 %, absolute gains up to 1 p.p. can be achieved. Thus, as demonstrated, the setup allows control and optimization of the TNR and TPR without manual tuning or cascading of sorters.

REFERENCES

[1] J. R. Mathiassen *et al.*, "Trends in Application of Imaging Technologies to Inspection of Fish and Fish Products," *Trends in Food Science & Technology*, vol. 22, no. 6, pp. 257–275, 2011.

[2] Y. J. Heo *et al.*, "Super-High-Purity Seed Sorter Using Low-Latency Image-Recognition Based on Deep Learning," *IEEE Robotics and Automation Letters*, vol. 3, no. 4, pp. 3035–3042, 2018.

[3] R. C. Bruce *et al.*, "The Impact of Optical Berry Sorting on Red Wine Composition and Sensory Properties," *Foods*, vol. 10, no. 2, p. 402, 2021.

[4] E. Gülcan and Ö. Y. Gülsoy, "Performance Evaluation of Optical Sorting in Mineral Processing – A Case Study with Quartz, Magnesite, Hematite, Lignite, Copper and Gold Ores," *International Journal of Mineral Processing*, vol. 169, pp. 129–141, 2017.

[5] C. Robben and H. Wotruba, "Sensor-Based Ore Sorting Technology in Mining—Past, Present and Future," *Minerals*, vol. 9, no. 9, p. 523, 2019.

[6] S. P. Gundupalli *et al.*, "A Review on Automated Sorting of Source-Separated Municipal Solid Waste for Recycling," *Waste Management*, vol. 60, pp. 56–74, 2017.

[7] B. Küppers *et al.*, "Influence of Material Alterations and Machine Impairment on Throughput Related Sensor-Based Sorting Performance," *Waste Management & Research: The Journal for a Sustainable Circular Economy*, vol. 39, no. 1, pp. 122–129, 2021.

[8] J. Sousa *et al.*, "Automation of Waste Sorting with Deep Learning," in *2019 XV Workshop de Visão Computacional (WVC)*. São Bernardo do Campo, Brazil: IEEE, 2019, pp. 43–48.

[9] G. Maier *et al.*, "Experimental Evaluation of a Novel Sensor-Based Sorting Approach Featuring Predictive Real-Time Multiobject Tracking," *IEEE Transactions on Industrial Electronics*, vol. 68, no. 2, pp. 1548–1559, 2021.

[10] J. Thumm *et al.*, "Mixture of Experts of Neural Networks and Kalman Filters for Optical Belt Sorting," *IEEE Transactions on Industrial Informatics*, vol. 18, no. 6, pp. 3724–3733, 2022.

[11] K. Friedrich *et al.*, "Assessment of Technological Developments in Data Analytics for Sensor-Based and Robot Sorting Plants Based on Maturity Levels to Improve Austrian Waste Sorting Plants," *Sustainability*, vol. 13, no. 16, p. 9472, 2021.

[12] R. S. Fitzpatrick *et al.*, "CFD–DEM Modelling of Particle Ejection by a Sensor-Based Automated Sorter," *Minerals Engineering*, vol. 79, pp. 176–184, 2015.

[13] C. Pieper *et al.*, "Numerical Modelling of an Optical Belt Sorter Using a DEM–CFD Approach Coupled with Particle Tracking and Comparison with Experiments," *Powder Technology*, vol. 340, pp. 181–193, 2018.

[14] G. Pajunen, "Adaptive Control of Wiener Type Nonlinear Systems," *Automatica*, vol. 28, no. 4, pp. 781–785, 1992.

[15] D. P. Bertsekas, *Dynamic Programming and Optimal Control*, 4th ed. Belmont, Massachusetts: Athena Scientific, 2017, vol. 1.